RSC Advances

PAPER

View Article Online
View Journal | View Issue

Cite this: *RSC Adv.*, 2015, **5**, 43449

Highly luminescent, off-stoichiometric $Cu_xIn_yS_2$/ZnS quantum dots for near-infrared fluorescence bio-imaging†

Hyung Seok Choi,‡[a] Youngsun Kim,‡[a] Jae Chul Park,‡[a] Mi Hwa Oh,[b] Duk Young Jeon*[ac] and Yoon Sung Nam*[abc]

Received 17th April 2015
Accepted 7th May 2015

DOI: 10.1039/c5ra06912b

www.rsc.org/advances

Quantum dots (QDs) are very attractive for *in vivo* bio-imaging and therapeutic applications due to their relatively large absorption coefficient, high quantum yield, low level of photo bleaching, and large Stokes shift. However, two technical issues need to be resolved before they can be practically applied to *in vivo* bio-imaging applications: ensuring both reduced toxicity and efficient emission in the near-infrared (NIR) frequency range. Here we report a simple and reliable method to synthesize highly luminescent, NIR-emitting $Cu_xIn_yS_2$/ZnS (CIS/ZnS) core–shell QDs for deep-tissue bio imaging applications. Off-stoichiometric effects are utilized with 1-dodecanethiol as a reaction medium for thermolytic synthesis. The most important finding in our work is that at a high Cu/In ratio, the emission spectrum of CIS/ZnS QDs can be tuned to NIR frequencies with a high quantum yield up to approximately 65%. The maximum emission wavelengths of the synthesized QDs are 589 nm (QD_{589}) and 726 nm (QD_{726}) at a Cu/In ratio of 0.25 and of 1.8, respectively. Their feasibility for optical bio-imaging in a deep-tissue condition is investigated by the intramuscular injection of QD-loaded polymer microspheres in a mouse model. Our results show that more than 30% of the original emission of the QD_{726} can be detected through biological tissue of 0.9 cm, whereas emission from the QD_{589} is not detectable. Our investigation on the off-stoichiometric effects of CIS QDs will contribute to the development of highly luminescent, NIR-emitting, cadmium-free QDs in the areas of tissue-level imaging, sensing, and therapeutics.

Introduction

Optical imaging techniques with advanced functions, such as rapid acquisition, high resolutions, and non-invasiveness, are the subject of increasing attention in relation to biomedical applications.[1,2] To achieve such functions, it is very important to develop not only a high-performance optical apparatus but also high-quality, functional optical materials. Semiconductor nanocrystals, often called quantum dots (QDs), have been widely studied as an advanced optical agent. The advantages of QDs over commonly used organic dyes include tunable emission spectra, high quantum yields, photochemical stability, and broad excitation spectra.[3–6] However, typical cadmium-based II–VI QDs (*e.g.*, CdS, CdSe, and CdTe) exhibit intrinsic toxicity, limiting their applicability for *in vivo* bio-imaging.[7] Ternary I–III–VI_2 QDs have attracted a considerable amount of attention as an alternative to cadmium-based QDs given their low toxicity and good optical properties.[8] In particular, $Cu_xIn_yS_2$ (CIS) QDs have a large absorption coefficient, large Stokes shifts, and high photostability.[9]

Various synthetic methods for CIS-based QDs have been reported, including a hot-injection process, solvothermal synthesis, and the thermal and photochemical decompositions of precursors.[10–15] Recent studies have shown that CIS/ZnS core–shell QDs can have a very high photoluminescence quantum yield (PLQY) of about 90% at 620 nm when synthesized by means of solvothermal synthesis in an octadecene-free condition with 1-dodecanethiol (DDT) as a sulfur source, a surface ligand, and a reaction medium.[16] However, their fluorescence emission was found to be limited to only visible light frequencies. Unfortunately, thus far no synthetic procedures have been reported for near-infrared (NIR)-emitting CIS-based QDs with a high PLQY (>60%). The NIR wavelength (700–900 nm) is considered to be the optimum spectral range for optical bio-imaging because scattering and absorption, which are caused by proteins, lipids, and

[a]*Department of Materials Science and Engineering, Korea Advanced Institute of Science and Technology, 291 Daehak-ro, Yuseong-gu, Daejeon, 305-701, Republic of Korea. E-mail: dyj@kaist.ac.kr; yoonsung@kaist.ac.kr*

[b]*Department of Biological Sciences, Korea Advanced Institute of Science and Technology, 291 Daehak-ro, Yuseong-gu, Daejeon, 305-701, Republic of Korea*

[c]*KAIST Institute for NanoCentury (CNiT), Korea Advanced Institute of Science and Technology, 291 Daehak-ro, Yuseong-gu, Daejeon, 305-701, Republic of Korea*

† Electronic supplementary information (ESI) available: Size distribution histograms of the CIS QDs (Fig. S1); comparison of PLQY with a previous work (Fig. S2); the original curve of absorption spectra of the CIS QDs (Fig. S3); size distribution histograms of the CIS/ZnS QDs (Fig. S4); SEM images of the QD-loaded PMMA microspheres (Fig. S5). See DOI: 10.1039/c5ra06912b

‡ These authors equally contributed to this work.

water, are minimized.[17,18] Therefore, if the emission spectra of CIS-based QDs can be extended to the NIR frequencies, an excellent candidate will be realized for *in vivo* bio-imaging with efficient optical penetration into deep tissues.

Several approaches have been tried to modulate the emission spectra of CIS QDs toward NIR while maintaining efficient photoluminescence. Because CIS has an excitonic Bohr diameter of about 8.2 nm and a direct bandgap of approximately 1.5 eV, size control essentially becomes a possible route for the fine-tuning of the emission spectra of CIS QDs. However, the optical properties of CIS QDs are greatly influenced by the presence of both of the internal and surface defects. The radiative carrier recombination process is driven by the intragap defect states, resulting in relatively large Stokes shifts. Therefore, to induce the spectral shift of CIS QDs toward the NIR region, it is important to control the internal defects, which are greatly affected by the stoichiometry of copper and indium ions.[19–24] However, only a few studies have reported a PLQY of more than 20% for CIS/ZnS QDs in the NIR region.[25,26] These values are far from sufficient for practical bio-imaging applications.[19,23,27] Non-radiative recombinations that originate from surface defects are considered as a major cause of such low PLQYs.[14,28–30] Therefore, both the stoichiometry of CIS QDs and the minimization of surface defects need to be considered to develop NIR-emitting CIS-based QDs with a high PLQY.

In this work, we report on a facile route for the synthesis of highly luminescent CIS/ZnS core–shell QDs with a PLQY of more than 50% in the NIR range. A simple heating-up method was utilized with DDT as a multi-functional agent, *i.e.*, a reaction medium, a sulfur source, and a capping ligand. No other organic solvents (*e.g.*, octadecene) or ligands except for DDT were used in our work. The structural, chemical, and optical properties of the synthesized CIS and CIS/ZnS QDs were examined. *In vitro* and *in vivo* feasibility tests for deep-tissue bio-imaging with the synthesized CIS/ZnS QDs were also conducted using a tissue-like phantom and a mouse model with an intramuscular administration.

Experimental

Chemicals and materials

Copper iodide (CuI, trace metals basis, 99.999%), indium acetate ($In(Ac)_3$, trace metals basis, 99.99%), DDT (98%), zinc undecylenate (98%), octadecene (90%), intralipid emulsion (20%), hemoglobin from bovine blood (a substrate powder), sodium chloride (99%), Trizma base (99.9%), sodium azide (NaN_3, 99.5%), gelatin from bovine skin (type B, powder), human serum albumin (HSA, purity $\geq$ 96%), and polyvinyl alcohol (PVA) (M_w = 146–186 kDa, 88% hydrolyzed) were purchased from Sigma-Aldrich (St. Louis, MO, USA). Poly(methyl methacrylate) (PMMA) with a nominal molecular weight of about 50 kDa was obtained from Kimex Co., Ltd (Suwon, Republic of Korea).

Synthesis of CIS/ZnS core–shell QDs

CIS QDs with different feeding ratios of Cu to In (0.25, 0.5, 1.0, and 2.0) were synthesized by controlling the concentration of CuI with a fixed concentration of $In(Ac)_3$. Both of CuI and $In(Ac)_3$ were dissolved in 20 mL of DDT and added to a 50 mL three-necked flask. The reaction mixture was magnetically stirred at 70 °C while it was degassed under a vacuum for 1 h and then purged with argon gas (ultra-high purity, 99.999%). The temperature was subsequently raised to 180 °C at a rate of 10 °C min^{-1}. The reaction temperature was maintained for 10 h. To synthesize a ZnS shell, 861.5 mg (2 mmol) of zinc undecylenate was dissolved in 8 mL of octadecene. The mixture was degassed for at least 15 min, refilled with argon gas, and then injected in a dropwise manner at a rate of 2 mL min^{-1} into the suspension of CIS QDs at 200 °C using a syringe pump (5 mL, NORM-JECT). After ZnS passivation, the heating mantle was removed, and the solution was cooled to 60 °C. The resulting CIS/ZnS core–shell QDs were purified by centrifugation in a mixture of methanol and chloroform (11 000×*g*) at 25 °C for 5 min. The precipitates were dispersed in chloroform and kept in the dark at room temperature until use.

Characterization

The absorption spectra were measured using an UV-vis spectrophotometer (UV-1800, Dong-il Shimadzu Corporation, Seoul, Republic of Korea). The photoluminescence (PL) spectra were measured using an F-7000 fluorescence spectrophotometer (Hitachi High-technologies, Tokyo, Japan) with an excitation wavelength of 370 nm. Size and structural characterization were obtained from transmission electron microscopy (TEM, JEOL JEM-3010, Tokyo, Japan) images with energy dispersive X-ray spectra (EDS) at an acceleration voltage of 200 kV. The crystal structures were determined by an X-ray diffraction analysis (XRD, D/MAX-2500/PC, Rigaku, Tokyo, Japan). The simulated $CuInS_2$ powder XRD patterns were obtained by using Diamond 3.0.[31] The chemical compositions were analyzed using inductively coupled plasma atomic emission spectroscopy (ICP-AES, iCAP 6300, Thermo Scientific, Rochester, USA). The fluorescence decay lifetime was measured using a fluorescence lifetime spectrometer (FL920, Edinburgh Instruments, UK).

In vitro imaging

Tris-buffered saline (TBS, 50 mM Trizma base and 150 mM sodium chloride) was used as a buffered solution (pH 7.4) for the tissue-like phantoms.[32] Sodium azide was added to the TBS to form 0.1 wt% TBS/azide. Ten grams of gelatin were suspended in 100 mL of TBS and autoclaved at 45 °C for 30 min, with continuous stirring until the gelatin was completely dissolved. The TBS with the gelatin was then cooled to 25 °C, and 10.9 g (170 μM) of bovine hemoglobin and 1 g of intralipid were added to the gelatin solution under magnetic stirring. The mixture was poured into a mold and allowed to solidify at 4 °C. To prepare an emitting layer, 1 mL of a CIS/ZnS QD solution (10 mg mL^{-1} in chloroform) was added to a 1 mL gelatin/TBS solution instead of bovine hemoglobin and intralipid. An *in vitro* imaging sensitivity test was conducted by stacking tissue-like phantoms on the emitting layer. Six phantom layers were stacked on one emitting layer. The degree of imaging sensitivity was

calculated by comparing the fluorescence intensity of initial emitting layer and the phantom-stacked emitting layer. The fluorescence images were captured with an IVIS® Lumina imaging system (Caliper Life Sciences, Hopkinton, MA, USA). The ROI (regions of interest) analysis was measured with Living Image® Software. The CCD exposure time was 2 s.

In vivo imaging

The CIS/ZnS QDs were encapsulated within PMMA microspheres by an oil-in-water single emulsification and solvent evaporation method.[33] Both the QDs (150 mg) and PMMA (1 g) were dissolved in 5 mL of methylene chloride. The resulting solution was injected all at once in 50 mL of a 0.3 wt% PVA aqueous solution and homogenized for 3 min at 2000 rpm, after which it was stirred magnetically for 12 h at room temperature to evaporate the methylene chloride. The QD-PMMA microspheres were collected by centrifugation for 10 min at 2000×*g* and washed several times with 50 mL of deionized water. Two female BALB/C nude mice (6 weeks of age, about 17 g) were housed one per cage in a pathogen-free environment. They were supplied with autoclaved and non-fluorescent mouse chow and water. All animal experiments were conducted in accordance with the guidelines provided by the Institutional Animal Care and Use committee of KAIST. The prepared QD-PMMA microspheres were dispersed in 0.2 mL of phosphate buffer saline (PBS, 137 mM NaCl and pH 7.4) and implanted intramuscularly into the posterior thigh muscle of a nude mouse with 2–3 mm in depth. For *in vitro* and *in vivo* imaging sensitivity tests, GFP (λ_{ex} = 445–490 nm and λ_{em} = 515–575 nm) and ICG (λ_{ex} = 710–760 nm and λ_{em} = 810–875 nm) excitation and emission filters were used for the visible light and NIR regions, respectively.

Results and discussion

The synthetic procedures used for the CIS/ZnS QDs are schematically described in Fig. 1. Typically, CuI and $In(Ac)_3$ were mixed with DDT in a three-necked flask. After degassing and backfilled with argon gas, the mixture was heated. The metal ions, Cu^+ and In^{3+}, can react with DDT to form transition metal–thiolate complexes, $(–Cu–SR–In–SR–)_n$ at 70 °C.[34] Thermal decomposition of the metal–thiolate complexes was carried out at 180 °C, leading to the nucleation of $CuInS_2$ clusters followed by growth. This reaction was indicated by a gradual evolution in the color from transparent yellow to bright orange, and finally to black, as the temperature increased. After additional Zn^{2+} ions were injected into the as-prepared CIS QDs, ZnS was epitaxially grown at 200 °C. The elemental compositions of the CIS QDs were analyzed by ICP-AES (Table 1). The measured Cu/In compositions were 0.25, 0.41, 1.1, and 1.8 for Cu/In feeding ratios of 0.25, 0.5, 1.0 and 2.0, respectively. This result indicates that the actual Cu/In ratios were similar to the feeding ratios for all of the prepared samples.

XRD diagrams of the synthesized CIS QDs with different Cu/In ratios of 0.25, 0.41, 1.1, and 1.8 are shown in Fig. 2A. The distinctive diffraction peaks with 2-theta values of 28.0°, 46.5°, and 54.9° can be assigned to the (111), (220), and (311) planes, respectively, of the cubic zinc blende structures.[31,35–38] The differences between the XRD pattern of zinc blende structure and that of chalcopyrite structure are only several minor peaks, which have low intensities. Therefore, it is very hard to distinguish the differences in their diffraction patterns, especially if the reflections are broadened because of the small sizes of the QDs.[20,35] In our work, the CIS QDs with different Cu/In ratios did not show any distinguishable differences in their diffraction patterns, indicating that the crystal structure was not greatly altered, even by the strong off-stoichiometric compositions. Compared to chalcopyrite $CuInS_2$, zinc blende $CuInS_2$ have a wider range of tunable Cu/In ratio because Cu^+ and In^{3+} ions can occupy the same position and have a random distribution in the zinc blende unit cell.[31,39] Therefore, it is reasonable to say that the synthesized CIS QDs have the zinc blende structure. TEM images of the CIS QDs with different compositions are shown in Fig. 2B. The HRTEM images shown in the inset show

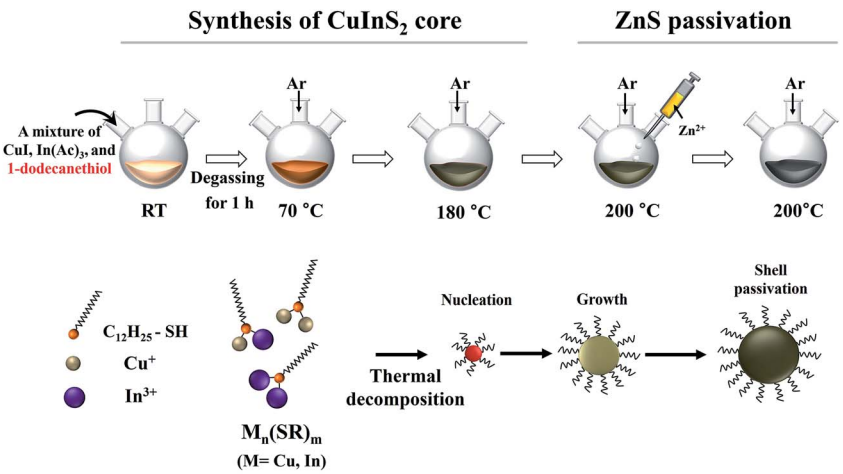

Fig. 1 Schematic description of the synthetic procedures of CIS/ZnS QDs by a heating-up method using DDT as a reaction medium as well as a sulfur source.

Table 1 Elemental compositions and optical properties of the synthesized CIS QDs

$[Cu/In]^a$	1.8	1.1	0.41	0.25
$[Cu/In]_{feeding}{}^b$	2.0	1.0	0.5	0.25
Absorption peak (nm)	N/A	551	482	449
PL peak (nm)	823	719	641	652
PLQY (%)	8.6	7.9	7.3	9.2
FWHM (nm)	105	148	116	134

[a] The molar ratio of Cu to In in the final products as measured by ICP-AES. [b] The molar ratio of Cu to In added to the reaction mixture.

the high crystallinity of the synthesized CIS QDs, with an average diameter (d, shown above the TEM images) of approximately 3 nm with a narrow size distribution (Fig. S1†). The observed distance of the lattice fringes of the CIS QDs ranged from 0.319 nm to 0.326 nm, which were very close to the d-spacing of the (111) planes for zinc blende $CuInS_2$. The increased d-spacing between the (111) planes increased with the increased Cu/In ratio. This tendency is very similar to the reported results of a previous study.[23] The origin of diffraction peak shifts seems to be related to a crystal distortion due to the generation of intrinsic defects. Because the bond length of In–S is about 5% larger than that of the Cu–S bond, the presence of intrinsic defects, such as Cu-on-In antisite defects, can induce crystal distortion.

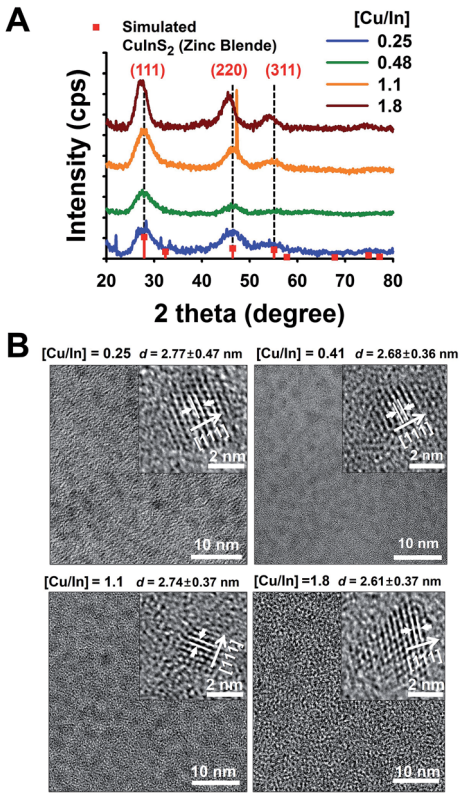

Fig. 2 XRD diagrams (A) and TEM images (B) of the CIS QDs synthesized with different compositions.

The normalized absorption and emission spectra of CIS QDs with various Cu/In ratios are shown in Fig. 3. Interestingly, despite no significant changes in the size and structure, the Cu/In ratio greatly affected the optical properties of the QDs. With an elevated ratio of Cu to In, the shoulder peak of the absorption spectra shifted from 449 nm to 551 nm. In the Cu-rich QDs, the shoulder peak was broadened ([Cu/In] = 1.1) and disappeared ([Cu/In] = 1.8), while the absorption level in the visible range to the NIR frequency increased broadly. In the PL spectra, the wavelength of the maximum PL peak was also shifted from the visible range ($\lambda_{em,peak}$ = 641.6 nm) to the NIR range ($\lambda_{em,peak}$ = 814.2 nm) as the Cu/In ratio increased. The red-shift and the spectral shape change of PL with respect to the increased Cu content can be ascribed to (i) the direct adjustment of the bandgap and (ii) the introduction of intragap defect states. In the Cu-rich composition, the repulsion between the d orbital of Cu and the p orbital of S is higher than that in Cu-deficient conditions, widening the gap between the bonding and anti-bonding states that constitute the valence band of the crystals.[40] This widening increases the valence band maximum such that the bandgap energy of the CIS QDs is reduced.[40,41] The aforementioned red shift of the absorption shoulder also supports this explanation. In addition, the high concentration of Cu species during the crystal growth causes defects, *i.e.*, Cu interstitials (Cu_i), Cu-to-In antisites (Cu_{In}), and In vacancies (V_{In}). A previous report on bulk CIS films suggests Cu_i as a deep-lying donor, Cu_{In} as a deep acceptor, and V_{In} as a shallow acceptor.[42] The deep trap transitions caused by the newly introduced defect pairs are attributed to the NIR emission in the Cu-rich CIS QDs. Therefore, the effects of Cu-rich compositions on the spectral changes of CIS QDs are likely caused by both of the direct change in the bandgap structures and the generation of intragap defect states. The photoluminescence of Cu-rich CIS QDs originates from the recombinations of electrons and holes trapped in the defect states (Fig. 4).[43]

The PLQY of the QDs was determined by comparing the total emission intensity of the QDs with that of rhodamine 6G at an excitation wavelength of 500 nm. The measured PLQYs of CIS QDs when Cu/In = 1.1, 0.41, and 0.25 were 7.9, 7.3, and 9.2%, respectively (Table 1). Previous studies showed that a Cu-rich composition resulted in a low level of fluorescence emission;[8,19,23] however, in the present work, it was found that the

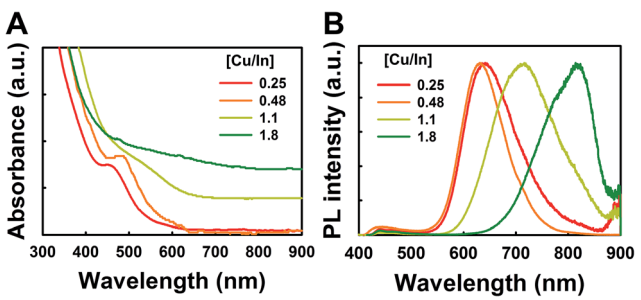

Fig. 3 Absorption (A) and PL (B) spectra of the CIS QDs synthesized with different Cu/In ratios at 180 °C. The excitation wavelength was fixed at 370 nm for PL measurements.

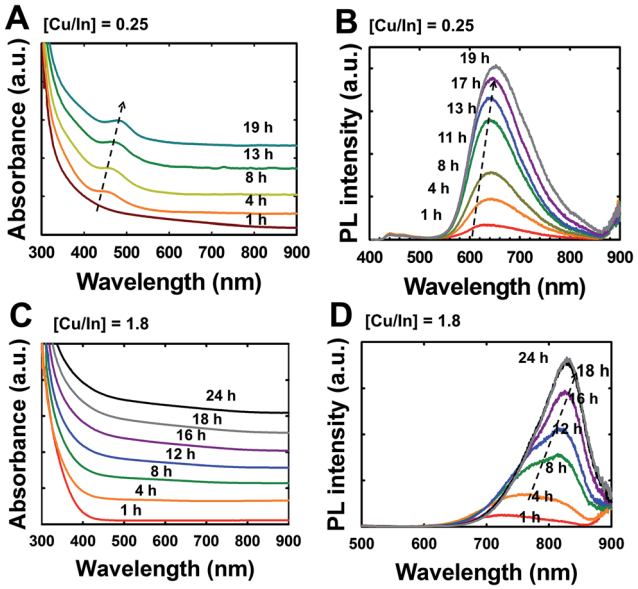

Fig. 4 Absorption (A and C) and PL (B and D) spectra of the CIS QDs with Cu/In ratios of 0.25 (A and B) and 1.8 (C and D) as a function of synthesis time at 180 °C. In the absorption spectra, the absorbance values of each curve at 900 nm were almost the same, but they were presented with increasing the level of base lines for easier comparison. The original curves are provided in the ESI (Fig. S3†). In the PL spectra, the excitation wavelength was 370 nm.

PLQY of the CIS QDs was not significantly dependent on the Cu/In ratio as shown in Fig. S2.† The PLQY of CIS QDs with a Cu-rich composition ([Cu/In] = 1.8) was 8.6% in the NIR region. Although the precise mechanism is not yet clear, the difference between the current work and the previous results could be related to the effect of the synthetic conditions on the deep-level defect population. In the DDT-only environment in our scheme, strong metal–thiolate complexes were always present at the growing edges of the crystals, almost perfectly passivating QDs while retarded the growth kinetics.[44,45] In this regime, intrinsic defects once created may scarcely migrate at the growing surface, prohibiting any annihilation or destructive interaction with the defects. Along with this effect, relatively a low growth temperature (*i.e.*, 180 °C) attenuates the diffusion of defect species and contributes to the surface passivation of QDs. As DDT acts as a stabilizing ligand during the reaction, its decomposition at a high temperature results in rapid destabilization of the colloids.[28,46] Therefore, in our low temperature and DDT-only synthesis, the surface of nanocrystals could be more effectively passivated by the ligands, which can reduce the surface defects that facilitate non-radiative decay, resulting in the high PLQY in the NIR region.

Although the synthesized CIS QDs exhibited fluorescence emission in the NIR region, the PLQY was less than 10%, requiring a further improvement for practical bio-imaging applications. To increase the PLQY of the CIS QDs, their surface was subsequently passivated with zinc sulfide (ZnS). ZnS has been widely used as a shell material for various QDs, including CIS QDs, owing to its similar crystal structure and a high bandgap energy (3.5 eV). The formation of a ZnS shell on CIS QDs was confirmed by XRD and TEM analyses as shown in Fig. 5. The size of QDs slightly increased as a result of the shell formation (Fig. S4†). The XRD patterns of the obtained CIS/ZnS QDs indicate the presence of the (111), (220), and (311) planes of zinc blende ZnS phase, and the clear lattice fringes in the HRTEM image indicate the crystalline nature of the resultant QDs.[47]

The formation of a ZnS shell layer on the CIS QDs offered a dramatic increase in the PLQY to both types of the two different stoichiometric CIS QDs (Fig. 6); the PLQY of the Cu-deficient QDs ([Cu/In] = 0.25) increased from 8.48% to 56.2%, and that of the Cu-rich QDs ([Cu/In] = 1.8) from 6.5% to 64.7%. This dramatic rise in the emission is ascribed to the effective surface passivation by the ZnS layer, reduced the surface trap sites on the CIS core.[48–50] Furthermore, we measured the PLQY of NIR-emitting QDs, which have an emission peak at 718.6 nm, using rhodamine B[49] to confirm the reliability of the PLQY determined with rhodamine 6G. Previous studies reported that the PL of rhodamine 6G is quenched in various solvents, including water, methanol, and ethanol,[50–52] which can be an extrinsic factor for the high PLQY of CIS/ZnS QDs. However, we found that the PLQY measured with rhodamine B was 45.9%, which is similar to that with rhodamine 6G (48.7%).[53,54] Therefore, the high PLQY of CIS/ZnS QDs was not derived from the PL quenching of rhodamine 6G, so the determined PLQY is reliable. During the ZnS passivation step, the size of the effective CIS core is reduced through the surface etching of the CIS core[30,48] or by the formation of an alloyed interfacial CIS/ZnS shell layer,[19,35,55] which can cause a blue shift of the absorption and emission peaks. The emission peak of the Cu-deficient QDs was shifted from 653.8 nm to 589.6 nm and the Cu-rich QDs also showed a blue shift from 786.2 to 726.6 nm. Park *et al.* reported that the degree of the blue shift *via* ZnS shell passivation increases proportionally to the increased PL emission peaks of CIS.[48] In this work, however, no significant difference in that degree was observed between Cu-deficient and Cu-rich QDs. This indicates that Cu-rich defects relevant to the NIR emission are well incorporated and are localized inside the core region of the CIS QDs in our synthetic scheme, despite the fact that some of them near the CIS surface and non-radiative defects appear to be annihilated during the ZnS shell passivation process.

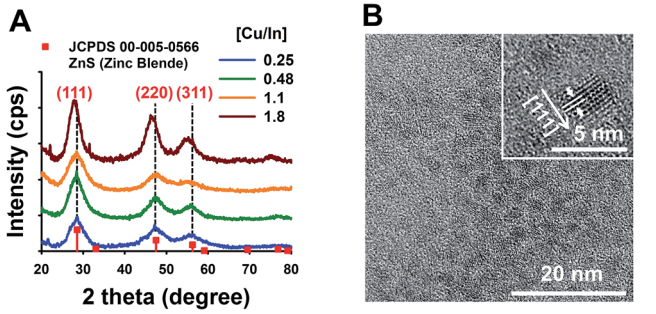

Fig. 5 (A) XRD diagrams of the CIS/ZnS QDs with different Cu/In ratios. (B) TEM images of CIS/ZnS QDs.

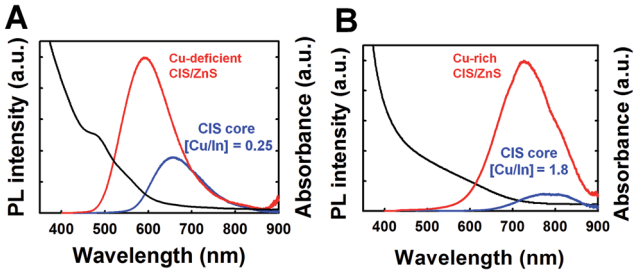

Fig. 6 Normalized absorption spectra and photoluminescence of the CIS/ZnS QDs from Cu-deficient (A) and Cu-rich (B) CIS QDs. The excitation wavelength was 370 nm for PL measurements.

Next, we determined the feasibility of the prepared NIR-emitting CIS/ZnS QDs as an imaging agent for deep-tissue imaging applications. The photon penetration efficiencies of the CIS/ZnS QDs with maximum emissions of 589 nm and 726 nm, denoted as 'QD_{589}' ([Cu/In] = 0.25) and 'QD_{726}' ([Cu/In] = 1.8), respectively, were determined by *in vitro* and *in vivo* methods. The PLQYs were 56.2% and 64.7% for QD_{589} and QD_{726}, respectively. For the *in vitro* tests, we prepared a tissue-like phantom, composed of gelatin, intralipid, and hemoglobin, with optical properties similar to cutaneous tissues. The imaging sensitivity levels of the QDs were measured by comparing the number of photons as a function of the number of phantom layers. The QDs were mixed with molten gelatin (10 mg mL^{-1}) to form a transparent QD-gelatin layer, called as 'a QD-emitting layer' (Fig. 7A). On top of the QD-emitting layer, 1.5 mm-thick layers of tissue-like phantoms were stacked in a layer-by-layer manner. The photon penetration percentage was 29.4% through six layers of phantom from the emitting layer of QD_{726}, while no photons were detected from the emitting layer of QD_{589} (Fig. 7B). For an *in vivo* sensitivity test, both QD_{589} and QD_{726} were encapsulated within PMMA microspheres prepared by an oil-in-water emulsification and solvent evaporation method.[32] The average diameter of the QD-loaded PMMA microspheres was 8.38 ± 6.46 μm, as determined by SEM (Fig. S5†). The QDs were encapsulated within the microspheres with encapsulation efficiencies of about 46%. The QD-loaded PMMA microspheres dispersed in PBS were implanted under the thigh muscle of a mouse by an intramuscular injection (0.2 mL). The fluorescence emission from the QD_{726} was clearly observed through mouse thigh muscles that were approximately 2 mm thick (Fig. 7D, right red circle), while no significant signal was detected from QD_{589} (Fig. 7C, left red circle). These results indicate that the NIR-emitting QD_{726} has much higher optical penetration efficiency through biological tissues.

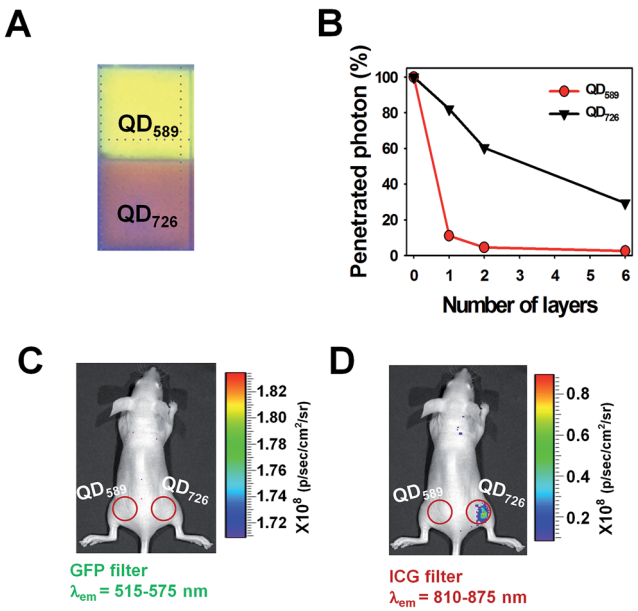

Fig. 7 The digital photograph of QD-emitting layer (A) and the photon penetration ratio of QD_{589} (λ_{max} = 589 nm) and QD_{726} (λ_{max} = 726 nm) using tissue-like phantoms (B). (C and D) The fluorescence images of the QD-loaded PMMA microspheres implanted into a thigh muscle by intramuscular injection. Imaged taken using a GFP excitation filter (445–490 nm) with a GFP emission filter (515–575 nm) (C) and an ICG emission filter (810–875) (D).

Conclusions

This study introduced a new facile method to synthesize cadmium-free, NIR-emitting CIS/ZnS core–shell QDs with a high PLQY of about 65%, and it demonstrated the feasibility of deep-tissue bio-imaging applications with these QDs. CIS/ZnS QDs were synthesized using a heating-up method with DDT as a reaction medium as well as a capping ligand. The synthesized QDs exhibited not only high PL emission but also tunable emission from yellow to the NIR region. Using *in vitro* and *in vivo* imaging sensitivity tests, QD_{726} was detectable at a depth of a few millimeters in a phantom and in an intramuscular section of a mouse. This study demonstrates the feasibility of less-toxic NIR CIS/ZnS QDs for bio-imaging applications in deeper tissues.

Conflict of interest

The authors declare no competing financial interest.

Acknowledgements

This work was supported by the National Research Foundation of Korea (NRF) Grant funded by the Korean Government (Ministry of Science, ICT and Future Planning, MSIP) (2012M3A7B4049802, 2013R1A1A1009626, and 2014M1A8A1049303).

Notes and references

1 R. G. Aswathy, Y. Yoshida, T. Maekawa and D. S. Kumar, *Anal. Bioanal. Chem.*, 2010, **397**, 1417–1435.
2 J. T. Wessels, A. C. Busse, J. Mahrt, C. Dullin, E. Grabbe and G. A. Mueller, *Cytometry, Part A*, 2007, **71**, 542–549.
3 M. Bruchez Jr, M. Moronne, P. Gin, S. Weiss and A. P. Alivisatos, *Science*, 1998, **281**, 2013–2016.

4 H. Mattoussi, J. M. Mauro, E. R. Goldman, G. P. Anderson, V. C. Sundar, F. V. Mikulec and M. G. Bawendi, *J. Am. Chem. Soc.*, 2000, **122**, 12142–12150.
5 X. Michalet, F. F. Pinaud, L. A. Bentolila, J. M. Tsay, S. Doose, J. J. Li, G. Sundaresan, A. M. Wu, S. S. Gambhir and S. Weiss, *Science*, 2005, **307**, 538–544.
6 I. L. Medintz, H. T. Uyeda, E. R. Goldman and H. Mattoussi, *Nat. Mater.*, 2005, **4**, 435–446.
7 T. Pons, E. Pic, N. Lequeus, E. Casette, L. Bezdetnaya, F. Guillemin, F. Marchal and B. Dubertret, *ACS Nano*, 2010, **4**, 2531–2538.
8 H. Zhong, Z. Bai and B. Zou, *J. Phys. Chem. Lett.*, 2012, **3**, 3167–3175.
9 K. Nose, T. Omata and S. Otsuka-Yao-Matsuo, *J. Phys. Chem. C*, 2009, **113**, 3455–3460.
10 H. Kim, H. S. Jang, B. Kwon, M. Suh, Y. Kim, S. H. Cheong and D. Y. Jeon, *Electrochem. Solid-State Lett.*, 2012, **15**, K16–K18.
11 J. H. Kim, W. S. Song and H. Yang, *Opt. Lett.*, 2013, **38**, 2885–2888.
12 P. M. Allen and M. G. Bawendi, *J. Am. Chem. Soc.*, 2008, **130**, 9240–9241.
13 H. Kim, M. Suh, B. H. Kwon, D. S. Jang, S. W. Kim and D. Y. Jeon, *J. Colloid Interface Sci.*, 2011, **363**, 703–706.
14 W. W. Xiong, G. H. Yang, X. C. Wu and J. J. Zhu, *ACS Appl. Mater. Interfaces*, 2013, **5**, 8210–8216.
15 Y. Chen, S. Li, L. Huang and D. Pan, *Nanoscale*, 2014, **6**, 1295–1298.
16 W. S. Song and H. Yang, *Appl. Phys. Lett.*, 2012, **100**, 183104.
17 R. Weissleder, *Nat. Biotechnol.*, 2001, **19**, 316–317.
18 M. G. Panthani, T. A. Kahn, D. K. Reid, D. J. Hellebusch, M. R. Rasch, J. A. Maynard and B. A. Korgel, *Nano Lett.*, 2013, **13**, 4294–4298.
19 M. Uehara, K. Watanabe, Y. Tajiri, H. Nakamura and H. Maeda, *J. Chem. Phys.*, 2008, **129**, 134709.
20 D. E. Nam, W. S. Song and H. Yang, *J. Colloid Interface Sci.*, 2011, **361**, 491–496.
21 D. E. Nam, W. S. Song and H. Yang, *J. Mater. Chem.*, 2011, **21**, 18220–18226.
22 L. D. Trizio, M. Prato, A. Genovese, A. Casu, M. Povia, R. Simonutti, M. J. P. Alcocer, C. D'Andrea, F. Tassone and L. Manna, *Chem. Mater.*, 2012, **24**, 2400–2406.
23 B. Chen, H. Zhong, W. Zhang, Z. Tan, Y. Li, C. Yu, T. Zhai, Y. Bando, S. Yang and B. Zou, *Adv. Funct. Mater.*, 2012, **22**, 2081–2088.
24 P. H. Chuang, C. C. Lin and R. S. Liu, *ACS Appl. Mater. Interfaces*, 2014, **6**, 15379–15387.
25 W. Guo, N. Chen, Y. Tu, C. Dong, C. Hu and J. Chang, *Theranostics*, 2013, **3**, 99–108.
26 R. Zhang, P. Yang and Y. Wang, *J. Nanopart. Res.*, 2013, **15**, 1910.
27 H. Zhong, Y. Zhou, M. Ye, Y. He, J. Ye, C. He, C. Yang and Y. Li, *Chem. Mater.*, 2008, **20**, 6434–6443.
28 H. Zhong, S. S. Lo, T. Mirkovic, Y. Li, Y. Ding, Y. Li and G. D. Scholes, *ACS Nano*, 2010, **4**, 5253–5262.
29 J. Kolny-Olesiak and H. Weller, *ACS Appl. Mater. Interfaces*, 2013, **5**, 12221–12237.
30 L. Li, A. Pandey, D. J. Werder, B. P. Khana, J. M. Pietryga and V. I. Klimov, *J. Am. Chem. Soc.*, 2011, **133**, 1176–1179.
31 D. Pan, L. An, W. Hou, Y. Yang and Y. Lu, *J. Am. Chem. Soc.*, 2008, **130**, 5620–5621.
32 A. M. De Grand, S. J. Lomnes, D. S. Lee, M. Pietrzykowski, S. Ohnishi, T. G. Morgan, A. Goqbashian, R. G. Laurence and J. V. Frangioni, *J. Biomed. Opt.*, 2006, **11**, 014007.
33 J. S. Lee, Y. S. Nam, B. Y. Kang, S. H. Han and I. S. Chang, *J. Appl. Polym. Sci.*, 2004, **92**, 517–522.
34 T. Kino, T. Kuzuya, K. Itoh, K. Sumiyama, T. Wakamatsu and M. Ichidate, *Mater. Trans.*, 2008, **49**, 435–438.
35 K. Nose, Y. Soma, T. Omata and S. Otsuka-Yao-Matsuo, *Chem. Mater.*, 2009, **21**, 2607–2613.
36 W. Yue, S. Han, R. Peng, W. Shen, H. Geng, F. Wu, S. Tao and M. Wang, *J. Mater. Chem.*, 2010, **20**, 7570–7578.
37 W. C. Huang, C. H. Tseng, S. H. Chang, H. Y. Tuan, C. C. Chiang, L. M. Lyu and M. H. Huang, *Langmuir*, 2012, **28**, 8496–8501.
38 Z. Liu, L. Wang, Q. Hao, D. Wang, K. Tang, M. Zuo and Q. Yang, *CrystEngComm*, 2013, **15**, 7192–7198.
39 Y. Chen, S. Li, L. Huang and D. Pan, *Inorg. Chem.*, 2013, **52**, 7819–7821.
40 S. B. Zhang, S. H. Wei, A. Zunger and H. Katayama-Yoshida, *Phys. Rev. B: Condens. Matter Mater. Phys.*, 1998, **57**, 9642–9656.
41 N. S. Orlova, I. V. Bodnar and E. A. Kudritskaya, *Cryst. Res. Technol.*, 1998, **33**, 37–42.
42 X. Liu, X. Dou and M. Sugiyama, *Jpn. J. Appl. Phys.*, 2012, **51**, 122403.
43 S. L. Castro, S. G. Bailey, R. P. Raffaelle, K. K. Banger and A. F. Hepp, *J. Phys. Chem. B*, 2004, **108**, 12429–12435.
44 D. W. Deng, Y. Chen, J. Cao, J. Tian, Z. Qian, S. Achilefu and Y. Gu, *Chem. Mater.*, 2012, **24**, 3029–3037.
45 R. Xie, M. Rutherford and X. Peng, *J. Am. Chem. Soc.*, 2009, **131**, 5691–5697.
46 W. Zhang and X. Zhong, *Inorg. Chem.*, 2011, **50**, 4065–4072.
47 J. Niu, W. Xu, H. Shen, S. Li, H. Wang and L. S. Li, *Bull. Korean Chem. Soc.*, 2012, **33**, 393–397.
48 J. Park and S. W. Kim, *J. Mater. Chem.*, 2011, **21**, 3745–3750.
49 J. Sun, D. Zhu, J. Zhao, M. Ikezawa, X. Wang and Y. Masumoto, *Appl. Phys. Lett.*, 2014, **104**, 023118.
50 Y. K. Kim, S. H. Ahn, K. Chung, Y. S. Cho and C. J. Choi, *J. Mater. Chem.*, 2012, **22**, 1516–1520.
51 A. M. Brouwer, *Pure Appl. Chem.*, 2011, **83**, 2213–2228.
52 F. L. Arbeloa, P. R. Ojeda and I. L. Arbeloa, *J. Chem. Soc., Faraday Trans. 2*, 1988, **84**, 1903–1912.
53 A. Penzkofer and Y. Lu, *Chem. Phys.*, 1986, **103**, 399–405.
54 F. L. Arbeloa, P. R. Ojeda and I. L. Arbeloa, *J. Photochem. Photobiol., A*, 1988, **45**, 313–323.
55 H. Kim, J. Y. Han, D. S. Kang, S. W. Kim, D. S. Jang, M. Suh, A. Kirakosyan and D. Y. Jeon, *J. Cryst. Growth*, 2011, **326**, 90–93.